




Adjusting the bow-tie: a morpho-kinematic study of NGC 40

J. B. Rodríguez-González ¹★, J. A. Toalá ¹, L. Sabin ², G. Ramos-Larios ³, M. A. Guerrero ⁴, J. A. López ² and S. Estrada-Dorado ¹

¹*Instituto de Radioastronomía y Astrofísica, UNAM Campus Morelia, Apartado postal 3-72, 58090 Morelia, Michoacán, Mexico*

²*Instituto de Astronomía, Universidad Nacional Autónoma de México (UNAM), Apdo. Postal 877, 22800 Ensenada, B.C., Mexico*

³*Instituto de Astronomía y Meteorología, CUCEI, Univ. de Guadalajara, Av. Vallarta 2602, Arcos Vallarta, 44130 Guadalajara, Mexico*

⁴*Instituto de Astrofísica de Andalucía, IAA-CSIC, Glorieta de la Astronomía S/N, Granada 18008, Spain*

Accepted 2022 June 22. Received 2022 June 21; in original form 2022 February 8

ABSTRACT

We present a comprehensive study of the ionization structure and kinematics of the planetary nebula (PN) NGC 40 (a.k.a. the Bow-tie Nebula). A set of narrow-band images obtained with the Alhambra Faint Object Spectrograph and Camera at the Nordic Optical Telescope are used to study the turbulent distribution of gas in the main cavity, the ionization stratification and the density of this PN. High-resolution Manchester Echelle Spectrograph observations obtained at 2.1m telescope of the San Pedro Mártir Observatory are used to unveil in great detail the kinematic signatures of all morphological features in NGC 40. The images and spectra suggest that NGC 40 had multiple mass ejections in its recent formation history. We found 4 jet-like ejections not aligned with the main axis of NGC 40 ($PA = 20^\circ$), some of them having pierced the main cavity along the SW–NE direction as well as the southern lobe. Using a tailor-made morpho-kinematic model of NGC 40 produced with SHAPE, we found that the main cavity has a kinematic age of 6500 yr and the two pairs of lobes expanding towards the N and S directions have an averaged age of 4100 ± 550 yr. NGC 40 thus adds to the group of PNe with multiple ejections along different axes that challenge the models of PN formation.

Key words: stars: evolution – stars: mass-loss – stars: winds, outflows – stars: Wolf–Rayet – planetary nebulae: general – planetary nebulae: individual: NGC 40.

1 INTRODUCTION

Planetary nebulae (PNe) are remnants of the late stages of stellar evolution of low- and intermediate-mass stars ($1 \lesssim M_i/M_\odot \lesssim 8$). These stars lose most of their initial masses when evolving through the asymptotic giant branch (AGB) phase, where they exhibit a slow and dense wind ($\dot{M} \lesssim 10^{-5} \text{ yr}^{-1}$; $v_{\text{AGB}} \approx 20 \text{ km s}^{-1}$; Ramstedt et al. 2020). They expel their outer layers and become post-AGB stars increasing their stellar temperature and developing thus a strong line-driven wind ($v_\infty = 500\text{--}4000 \text{ km s}^{-1}$; Guerrero & De Marco 2013) that compresses and heats the material previously ejected in the AGB stage. At the same time, they develop a UV photon flux that ionizes the material, giving birth to a PN (Kwok, Purton & Fitzgerald 1978; Balick 1987).

About ~ 20 per cent of the known PNe harbour central stars (CSPN) that do not display any hints of H in their atmospheres (Weidmann et al. 2020). These H-deficient stars exhibit strong emission lines of He, C, and O, very similar to the massive Wolf–Rayet (WR) stars of the C sequence (WC; e.g. Acker & Neiner 2003). Therefore, they are also classified under the same scheme, but using square brackets to distinguish them from their massive siblings (Crowther, De Marco & Barlow 1998).

PNe harbouring WR-type CSPN (hereinafter WRPNe) display some differences when compared to PNe harbouring H-rich CSPN. Generally, they seem to have higher N and C abundances suggesting that they are the descendants of more massive stars (see García-Rojas

et al. 2013), which means that they are preferentially found close to the Galactic plane (Corradi & Schwarz 1995; Peña, Rechy-García & García-Rojas 2013). Some authors have found that WRPNe exhibit a larger degree of turbulence and present larger expansion patterns than non-WRPNe (e.g. Medina et al. 2006; Jacob, Schönberner & Steffen 2013). These properties are easily explained in WRPNe by invoking the large momentum imprinted by the powerful line-driven winds from WR-type CSPN (Todt et al. 2015). They compress and accelerate the previously ejected AGB material much stronger than those of H-rich CSPN, enhancing the formation of hydrodynamical instabilities such as the Rayleigh–Taylor (e.g. Stute & Sahai 2006; Toalá & Arthur 2016).

Kinematic studies of PNe help us assess the effects of the powerful winds from their CSPNe, investigate the mass-loss ejection histories that gave birth to these objects and their interaction with the circumstellar medium (see e.g. Aller et al. 2021; Sabin et al. 2017; Ramos-Larios et al. 2018; Guerrero et al. 2021; Henney et al. 2021; and references therein). In this paper, we present a morpho-kinematic study of the WRPN NGC 40, also known as the Bow-tie Nebula, around the [WC]-type star HD 826 (Hiltner & Schild 1966).

The main structure of NGC 40 has a barrel-like shape with two pairs of lobes expanding towards the northern and southern directions (see Fig. 1). Its symmetry axis appears to have a position angle (PA) of 20° (Sabbadin & Hamzaoglu 1982; Chu, Jacoby & Arendt 1987). Ring-like features detected in optical and IR images have been reported to surround the main structure of NGC 40 (Corradi et al. 2004; Ramos-Larios, Phillips & Cuesta 2011). Deep optical images of NGC 40 reveal an extended clumpy halo that extends more than 2.2 arcmin (see fig. 1 in Toalá et al. 2019). Kinematical

* E-mail: j.rodriiguez@irya.unam.mx

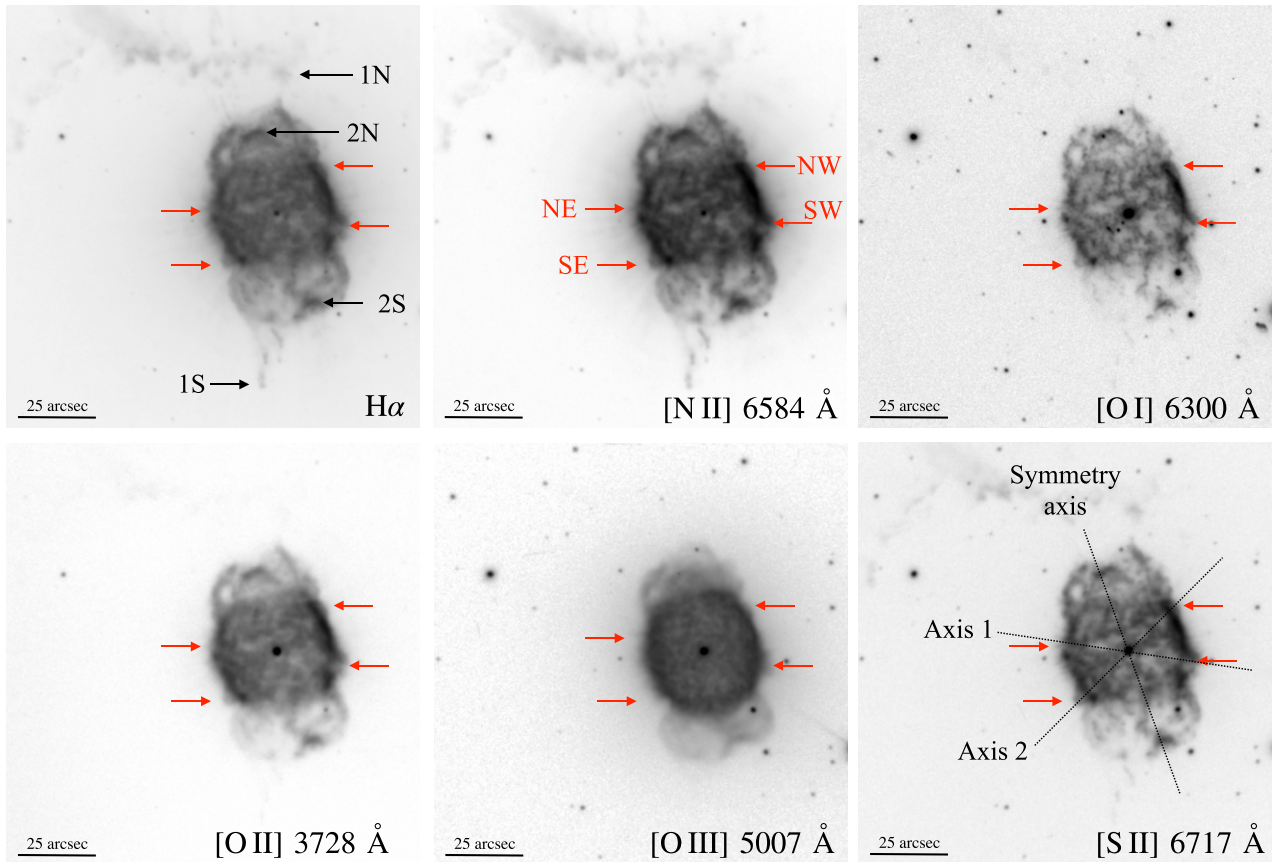


Figure 1. Narrow-band images of NGC 40 obtained with NOT ALFOSC. Each panel presents images in different emission lines. The position of the possible jet-like features 1N, 2N, 1S, and 2S are marked in the upper left-hand panel with black arrows. The two pairs of blowouts piercing the main cavity of NGC 40 are shown with red arrows in all panels (see the text for details). The bottom right-hand panel shows the symmetry axis of NGC 40 (PA = 20°). Axis 1 (PA = 80°) and 2 (PA = 135°) are defined by connecting the two pairs of blowouts protruding from the main cavity of NGC 40. All panels have the same field of view. North is up, east to the left.

studies of NGC 40 have suggested that its bipolar appearance is due to the possible action of bipolar ejections of material, jet-like features, oriented at PA \approx 0° and PA = 20° (Sabbadin & Hamzaoglu 1982; Meaburn et al. 1996).

In this paper, we present a 3D morpho-kinematic study of NGC 40 with the goal of unveiling the kinematical signature of possible different ejections from HD 826. High-resolution spectroscopic observations are used to peer into the formation scenario of NGC 40. These are interpreted by means of the 3D modelling tool for Astrophysics SHAPE (Steffen et al. 2011). We also investigate the ionization structure of NGC 40 by means of narrow-band imagery. This paper is organized as follows. In Section 2, we present the observations used in this paper. In Section 3, we describe our results. The morpho-kinematic SHAPE model is presented and compared to the observations in Section 4. The discussion and conclusions are presented in Sections 5 and 6, respectively.

2 OBSERVATIONS

We obtained optical images and spectra of NGC 40 from different telescopes. In the following, we describe the details of the observations. We note that all observations presented in this paper were processed using standard IRAF routines (Tody 1993).

2.1 NOT ALFOSC images

NGC 40 was observed on 2019 October 11 (Proposal ID 60-208, PI: M.A. Guerrero) with the Alhambra Faint Object Spectrograph and Camera (ALFOSC)¹ mounted at the Nordic Optical Telescope (NOT) at the Observatorio de El Roque de los Muchachos (ORM) in La Palma (Spain). Images were obtained using narrow-band filters centred on the H α , H β , [O I] λ 6300, [O II] λ 3727, [O III] λ 5007, [N II] λ 6584, and [S II] λ 6716,6731 emission lines. Broad-band images on the r' and g' filters were also obtained. Details of the observations such as filter, central wavelength (λ_c), FWHM, and total exposure time per filter are listed in Table 1. A selection of narrow-band images is presented in Fig. 1.

2.2 SPM MES spectra

NGC 40 was observed with the Manchester Echelle Spectrograph (MES; Meaburn et al. 2003) at the 2.1m telescope of the Observatorio Astronómico Nacional (OAN) in San Pedro Mártir (SPM) in Ensenada, México. The observations were performed through several runs between 2010 and 2019. A total of 60 high-resolution MES spectra were obtained at different positions and with different

¹<http://www.not.iac.es/instruments/alfosc/>

Table 1. Details of the narrow-band filters used for the NOT ALFOSC observations.

Filter	λ_c (Å)	FWHM (Å)	Exposure time (s)
[O II]	3728	32	600
H β	4854	133	1200
[O III]	5007	30	1200
[O I]	6300	30	1200
H α	6564	3.3	600
[N II]	6584	10	450
[S II]	6716	10	1200
[S II]	6731	10	1200
g'	4800	1450	30
r'	6250	1400	30

Table 2. Details of the spectroscopic data.

Instrument	Filter	λ (Å)	$\Delta\lambda$ (Å)	Season	Number of spectra	Exp. time (s)
MES SPM	H α	6580	90	2010 Aug	3	1200
		6580	90	2020 Sep	4	1200
		6580	90	2013 Sep	7	1800
		6580	90	2013 Dec	9	1800
		6580	90	2014 Jan	3	1800
		6580	90	2014 Oct	7	1800
	[S II]	6730	90	2019 Sep	9	1800
		6730	90	2019 Oct	18	1800
WHT UES	H α	6590	130	1995 Oct	1	600
	[O I]	6303	50	1995 Oct	1	600
	[O II]	3737	50	1995 Oct	1	600
	[O III]	5010	100	1995 Oct	1	600

filters. 33 spectra were acquired with the H α + [N II] interference filter with $\lambda_c = 6580$ and $\Delta\lambda = 90$ Å. This filter isolates the 87th order that includes the H α , He II 6560 Å, [C II] 6578 Å, and the [N II] 6548, 6584 Å doublet emission lines. In addition, we also obtained 27 spectra through the [S II] filter with $\lambda_c = 6730$ Å and $\Delta\lambda = 90$ Å that includes the [S II] 6716, 6731 Å doublet. Details of the observations are listed in Table 2. The slit positions are illustrated in Fig. 2.

2.3 WHT UES spectra

To complement our SPM-MES spectra, we also retrieved archival Utrecht Echelle Spectrograph (UES) observations.² The instrument was mounted on the William Herschel Telescope (WHT) also at ORM. The observations were obtained using a Tek 5 CCD detector with a spectral resolution of $R = 49\,000$ that corresponds to a velocity resolution of ~ 6 km s⁻¹.

The WHT UES observations were acquired in 1995 October 11 using the 3720, 5005, 6300, 6570, and 6705 Å filters, which include the H α + [N II], [O I], [O III] emission lines and the [O II] 3726, 3728 Å and [S II] 6716, 6731 Å doublets. All observation were taken with the same slit position covering the symmetry axis of NGC 40 (PA = 20°) across the CSPN. Observations details are also presented in Table 2.

3 RESULTS

3.1 Imaging

The narrow-band images of NGC 40 presented in Fig. 1 exhibit all the morphological features described in previous works (see fig. 3 in Meaburn et al. 1996): the main barrel-like cavity, the blister-like structures expanding towards the N-S with PA = 20°, and the northern filament extending along E-W, this one detected in the H α , H β (not shown here), [N II] and [S II]. Some marginal contribution to the [O I] narrow-band image is also detected.

Almost all narrow-band images have very similar morphologies, except for the [O I] and [O III], which trace the lowest and highest ionization structures in NGC 40, respectively. As discussed in Meaburn et al. (1996), the [O III] image has a more organized clumpy morphology than show in other filters, which are messier or more complex. Furthermore, the internal cavity detected in this image has a smaller extent (see fig. 11 in Meaburn et al. 1996). The [O III] image can be fitted by an ellipse with a semi-minor axis of 18 arcsec, whilst for the other narrow-band images an ellipse with a semi-minor axis of 20 arcsec is necessary.

The subtle morphological differences presented by the different narrow-band images of NGC 40 can be explained as the result of the combination of the current fast stellar wind ($v_\infty = 1000$ km s⁻¹; Toalá et al. 2019) and the ionizing UV flux. The current fast wind is sweeping the inner nebular material producing Rayleigh–Taylor instabilities (see e.g. Stute & Sahai 2006; Toalá & Arthur 2016), creating a more or less organized inner clumpy structure and at the same time the UV flux from HD 826 ionizes the material. The ionization flux is trapped in the densest knots producing the so-called shadowing instability (Williams 1999; Arthur & Hoare 2006). As a result, the ionization is not uniform through NGC 40 creating a more chaotic pattern of ionized structures for larger radii such as the low-ionization structure detected in the [O I] image. This is consistent with the streaks of alternating ionized material observed in the halo just outside the main cavity of NGC 40 revealed in deep optical and IR images (Corradi et al. 2004; Ramos-Larios et al. 2011).

An inspection of the narrow-band images disclose the presence of two pairs of blowouts located on the E and W walls of the main cavity of NGC 40. Their positions are marked in all panels of Fig. 1 with red arrows. The most evident are those blowouts located at the NW, SW, and SE edges of the central cavity. However, a fourth blowout can be identified after careful examination of the images on the NE part of this region. The pairs of blowouts break the main barrel-like structure of NGC 40 at PA $\approx 80^\circ$ and 135° . This situation is illustrated in the bottom right-hand panel of Fig. 1. It is interesting to note that the pair of blowouts in Axis 1 (PA = 80°) seem to have pierced through NGC 40, while those in Axis 2 (PA = 135°) seem to be currently disrupting the edge of the main cavity. Interestingly, the maxima of the X-ray emission detected by *Chandra* are also aligned with Axis 2 (see Montez et al. 2005).³

To study the relative variation of excitation and to assess the presence of shocked structures in NGC 40, we have created line ratio images from different narrow-band images. Before producing the ratio maps, we subtracted the continuum using the g' and r' broad-band images of NGC 40. Hence, for images obtained at longer wavelengths (H α , [N II], [O I], and [S II]), we have subtracted the r' filter, whilst for the rest of the images (H β , [O II], and [O III]) we have subtracted the g' broad filter. Examples of the ratio maps are

²The observations were retrieved from the Isaac Newton Group Archive at <http://casu.ast.cam.ac.uk/casuadc/ingarch/query>

³See also <https://chandra.harvard.edu/photo/2005/n40/>

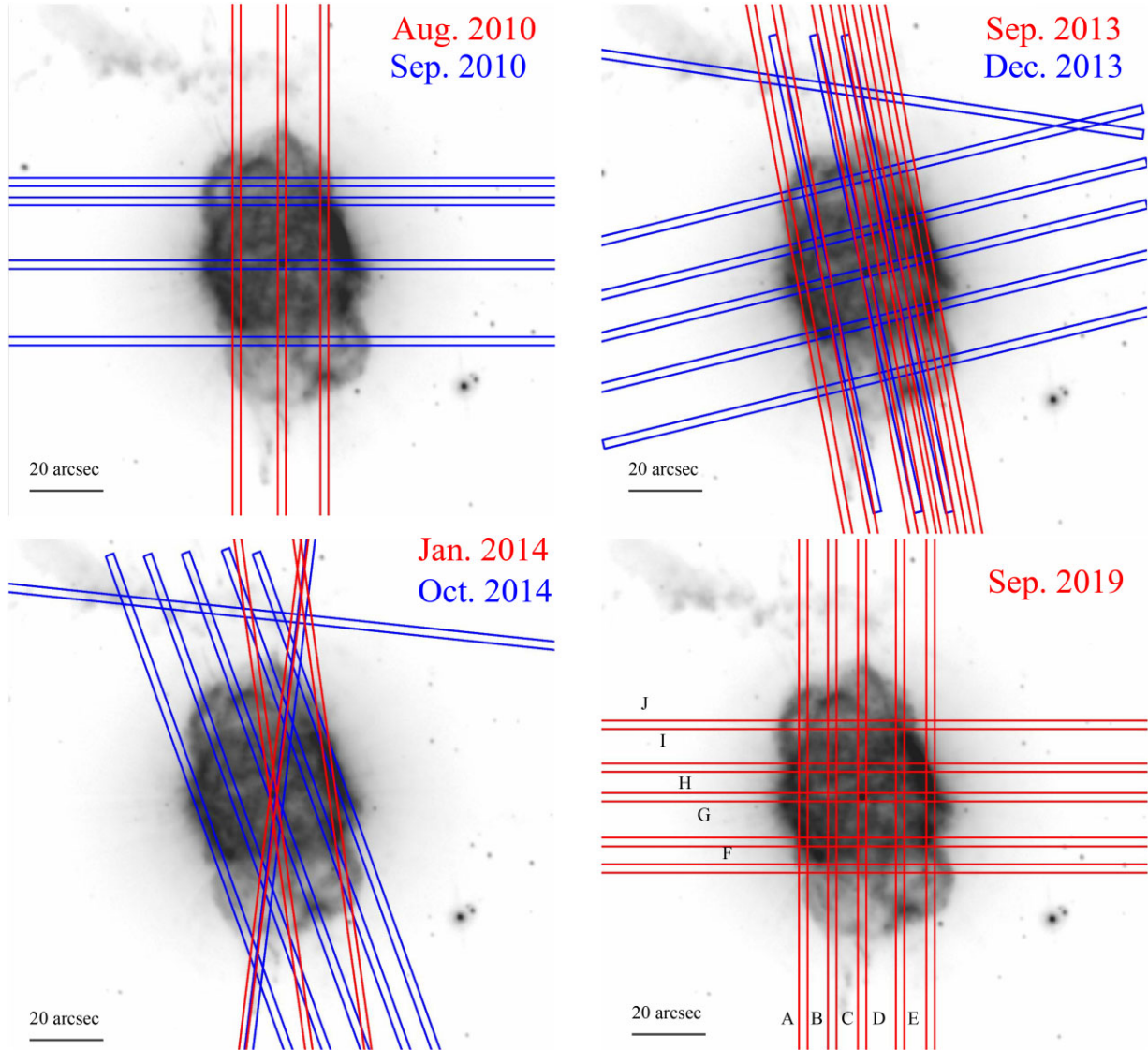


Figure 2. Narrow-band [N II] image of NGC 40 with the slit positions of the MES observations overplotted. The upper and lower-left panels show all the slits obtained with the spectroscopic configuration covering the H α and [N II] emission lines with different colours illustrating different observing runs. Similarly, the lower right-hand panel shows examples of the slit positions along key nebular features with the spectroscopic configuration covering the [S II] doublet.

presented in Fig. 3. We note that although the images are not flux-calibrated, they can still be used to describe in detail the ionization structure of NGC 40.

A fast outflow propagating into a low-density medium generates a forward shock that produces an increase in the electron temperature. This would increase the emission in the [O III] 5007 Å line, which is sensitive to T_e changes, while the low density would reduce the emissivity of the H α line, which is more sensitive to n_e . Consequently, the ratio [O III]/H α is expected to increase significantly in regions of shocked gas (Guerrero et al. 2008, 2013). The [O III]/H α ratio map (Fig. 3, top left-hand panel) shows that NGC 40 is delimited by a structure with relatively low values. Almost the entire nebula can be delineated with values [O III]/H $\alpha < 0.2$, which is due to the ionization stratification in NGC 40 with the [O III] structure contained within the H α -emitting region. There are certain directions, however, where the values of the [O III]/H α ratio increase, particularly along the direction of the SW blowout.

Within the main cavity of NGC 40 there are areas with values [O III]/H $\alpha > 0.6$, two corresponding to the N and S areas as well as an elongated structure that extends from the NW to the SE of the inner cavity where the blowouts align with Axis 1 (PA = 80°). A similar ionization structure is unveiled by the [O III]/[O II] map (Fig. 3, top right-hand panel).

An unprecedented view of NGC 40 is presented by the [O III]/[O I] ratio map (Fig. 3, bottom left-hand panel), which unveils its inner clumpy morphology. This image also discloses material extending beyond the main cavity of NGC 40, in particular the SW blowout along PA 260°, which traces ionized material streaking out from the western edge of the main cavity. The latter effect cannot be appreciated in the western region of the main cavity.

Finally, since we also have continuum-subtracted images of the [S II] 6716,6731 Å doublet, we calculated an electron density (n_e) map. For this, we used the PYNEB task *getTemDen* (Luridiana, Morisset & Shaw 2015) adopting the electron temperature of $T_e = 8200$ K as reported by Pottasch et al. (2003). The bottom right-hand

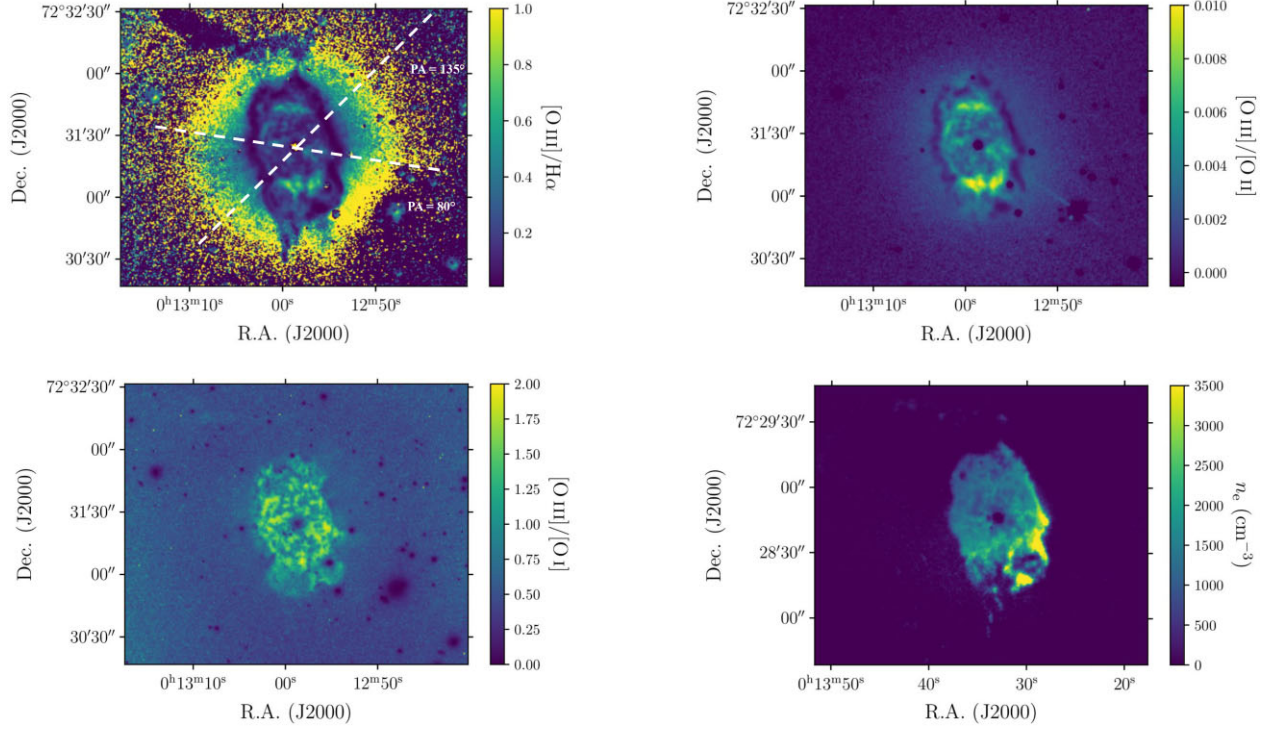


Figure 3. Ratio maps of different continuum-subtracted narrow-band images of NGC 40. The panels show the [O III]/H α (top-left), [O III]/[O II] (top-right), [O III]/[O I] (bottom-left). The bottom right-hand panel presents the electron density (n_e) map obtained from the [S II] 6716,6731 Å images using PYNEB.

panel of Fig. 3 presents the resultant n_e map that shows that NGC 40 has values around 1000 and 2000 cm^{-3} with some areas with higher n_e found in the SW regions and indicating electronic densities $n_e \gtrsim 3500 \text{ cm}^{-3}$. Our n_e map is consistent with the n_e values reported in previous works (see e.g. Clegg et al. 1983; Pottasch et al. 2003; Leal-Ferreira et al. 2011, and references therein).

3.2 Spectra

We created position–velocity (PV) diagrams for all spectra presented in this paper, although only a selection of the large number of PV diagrams derived from the SPM-MES observations are shown for simplicity. In Fig. 4, we present the [N II] 6584 Å PV diagrams corresponding to observations performed on 2013 December, while in Fig. 5 we present those of the [S II] 6716 Å obtained on 2019 September and October. Fig. 6 shows the corresponding PV diagrams from the WHT UES observations. All spectra were corrected from Local Standard Rest (LSR) using the IRAF *rvcorrect* task and are plotted with respect to systemic velocity, which was determined to be -25 km s^{-1} using H α and [N II] spectra profile at the position of the central star.

In order to obtain expansion velocities (v_{exp}), we performed Gaussian fits to the different components in the PV diagrams. The expansion velocity obtained from the [N II] spectra taken along the minor axis of the central cavity of NGC 40, for example slit C in Fig. 4, resulted in $v_{\text{exp}} = 25 \text{ km s}^{-1}$. Spectra obtained using the symmetry axis, such as slit G in Fig. 4, resulted in an expansion velocity $v_{\text{exp}} = 22 \text{ km s}^{-1}$. The expansion velocity of the northern lobes was found to be $v_{\text{exp}} = 13 \text{ km s}^{-1}$, while the ones in the southern region of the main cavity resulted in $v_{\text{exp}} = 10 \text{ km s}^{-1}$. The PV of the filamentary structure located at the north from NGC 40 (slit I in Fig. 4) does not show a relevant velocity. Most of this filament appears to be located at the same velocity of the CSPN of NGC 40

($v_{\text{LSR}} \approx 0 \text{ km s}^{-1}$) with a small velocity gradient of 5 km s^{-1} from the NW part of this structure.

The UES spectra were obtained for different emission lines at the same PA = 20° (the symmetry axis), therefore, giving us the advantage of studying the kinematics of NGC 40 taking into account the ionization structure. Spectra of H α , [N II] $\lambda\lambda 6548, 6584$, [O I] $\lambda\lambda 6300, 6363$, [O II] $\lambda 3726, 3729$, and [O III] $\lambda\lambda 4957, 5007$ emission lines were obtained. The profiles have similar shapes except for the [O III] emission lines, similarly to the situation with the narrow-band images, the later exhibits a clumpier structure and it is definitely contain within the rest of the structures. An expansion velocity of this structure of 30 km s^{-1} was obtained for the spectrum of [O III], while expansion velocities of 24 and 26 km s^{-1} were obtained for the [N II] and [O II] spectra, respectively. The slowest expansion is seen in the spectrum of [O I] with 17.7 km s^{-1} , which corresponds to the outermost structures in NGC 40.

It is interesting to mention that we detect a pair of red-shifted high-speed components in the [O III] PV diagram projected on to the main cavity. We marked these components with (white) arrows in the rightmost panel of Fig. 6. A close-up of the [O III] PV diagram presented in Fig. 7 shows that they have velocities of 60 km s^{-1} for the northern component and 66 km s^{-1} for the southern one, located 17 arcsec and 13.8 arcsec from the central star, respectively. Additional high-velocity features might be present at other spatial locations in the [O III] PV diagram, but their low signal-to-noise (S/N) renders their detection questionable.

4 A MORPHO-KINEMATIC MODEL

To interpret the SPM MES observations in order to determine the true structure of NGC 40 and to investigate its formation history, we have used SHAPE. This software is used to reconstruct and model the morpho-kinematic signatures of astrophysical objects.

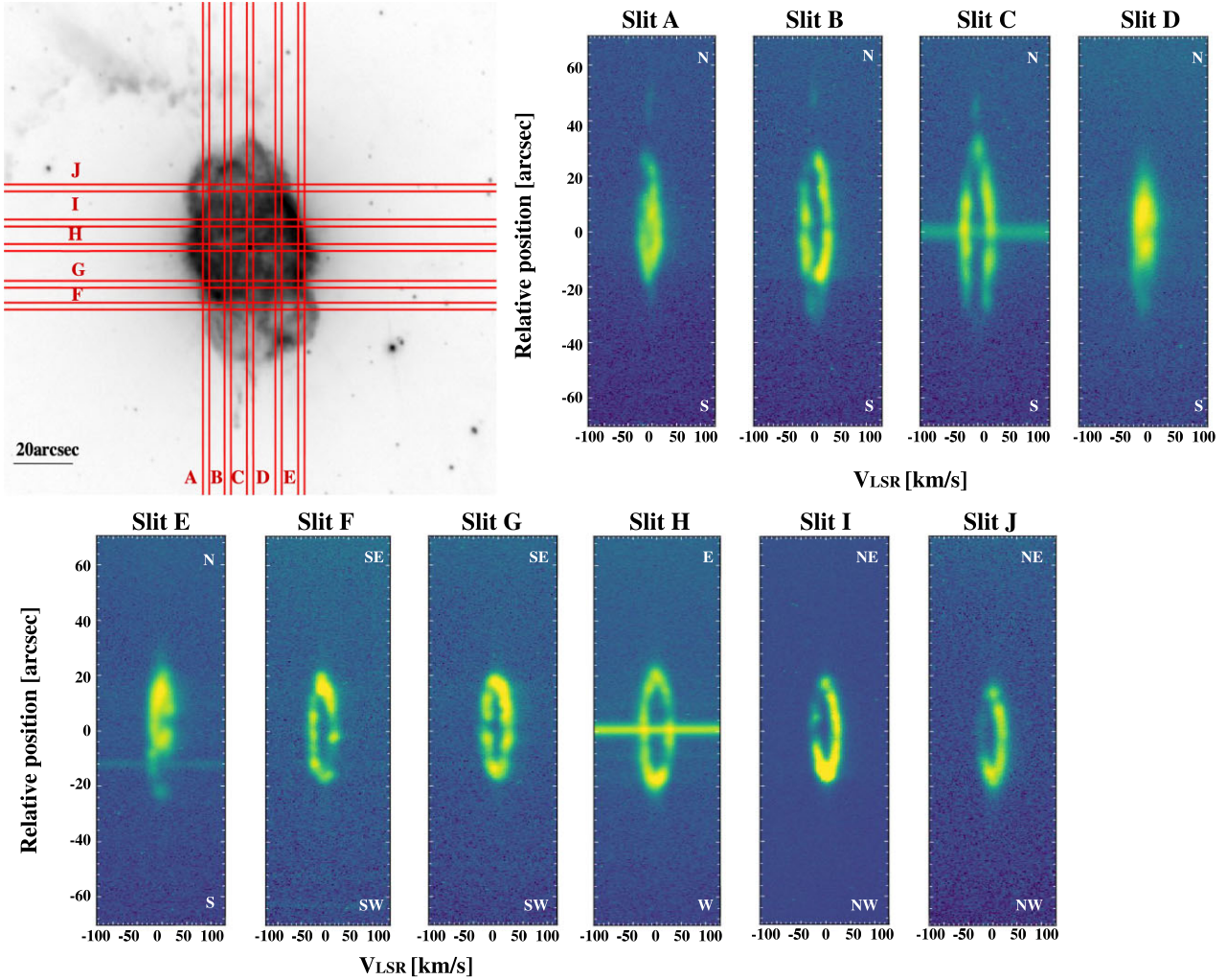


Figure 4. SPM MES [N II] 6584 Å spectra of NGC 40 obtained during 2013 December.

This procedure will be applied to NGC 40 by comparing synthetic PV diagrams and images with those obtained from observations. We note that the bulk of material is detected through the H α and [N II] emission lines, but the latter suffers from much less thermal broadening. Thus, we will use SHAPE to create synthetic PV diagrams that will be directly compared with those obtained from the [N II] $\lambda 6584$ Å SPM MES spectra, which is then assumed to describe the general formation scenario of NGC 40.

We started by including a barrel-like component to reproduce the main structure. The PA of the main axis of the barrel-like structure is chosen to be 20° , as suggested by the symmetry axis of NGC 40. This structure has a semimajor and semiminor axis of 13 and 20 arcsec with a thickness of 8 arcsec. To reproduce the PV diagrams crossing over the main cavity of NGC 40, the SHAPE model requires the barrel-like structure to have an expansion velocity of 25 km s^{-1} .

Given the complexity of NGC 40 revealed by the narrow-band images, we added additional structures. The northern and southern lobes protruding from the main structure are modelled by including two pairs of cap structures. The northern and southern pairs of caps are modelled using truncated spheres. The northern pair of caps has averaged radii of 8 with thickness of 7 arcsec. The southern pair of caps is slightly larger than the northern ones, with averaged radii of 10 arcsec and thickness of 5 arcsec. To reproduce the SPM MES

spectra passing through the lobes, the model required expansion velocities of the northern and southern caps of 26 and 15 km s^{-1} , respectively. Details of these structures are listed in Table 3.

We present in Fig. 8 the visualization of our SHAPE model. The clumpy structure of NGC 40 unveiled by the narrow-band images are simulated adding noise to the model. Additional clumps have been added in the model to the NW and SE regions of the barrel-like cavity to reproduce its higher brightness. The synthetic image of NGC 40 created from the morpho-kinematics reconstruction makes a good job reproducing most of the narrow-band images presented in previous sections.

Synthetic PV diagrams obtained from our SHAPE model of NGC 40 are presented in Fig. 9. These are compared side by side with the SPM MES observations obtained on December 2013, which are representative of the kinematics of NGC 40, as they cover its main structures. Our model reproduces fairly well the observed [N II] $\lambda 6584$ Å PVs obtained from different slit positions.

5 DISCUSSION

The high-quality NOT images of NGC 40 presented here allowed us to unveil the ionization structure of this PN with unprecedented detail. There are noticeable similarities between the H α , H β , [N II], [S II],

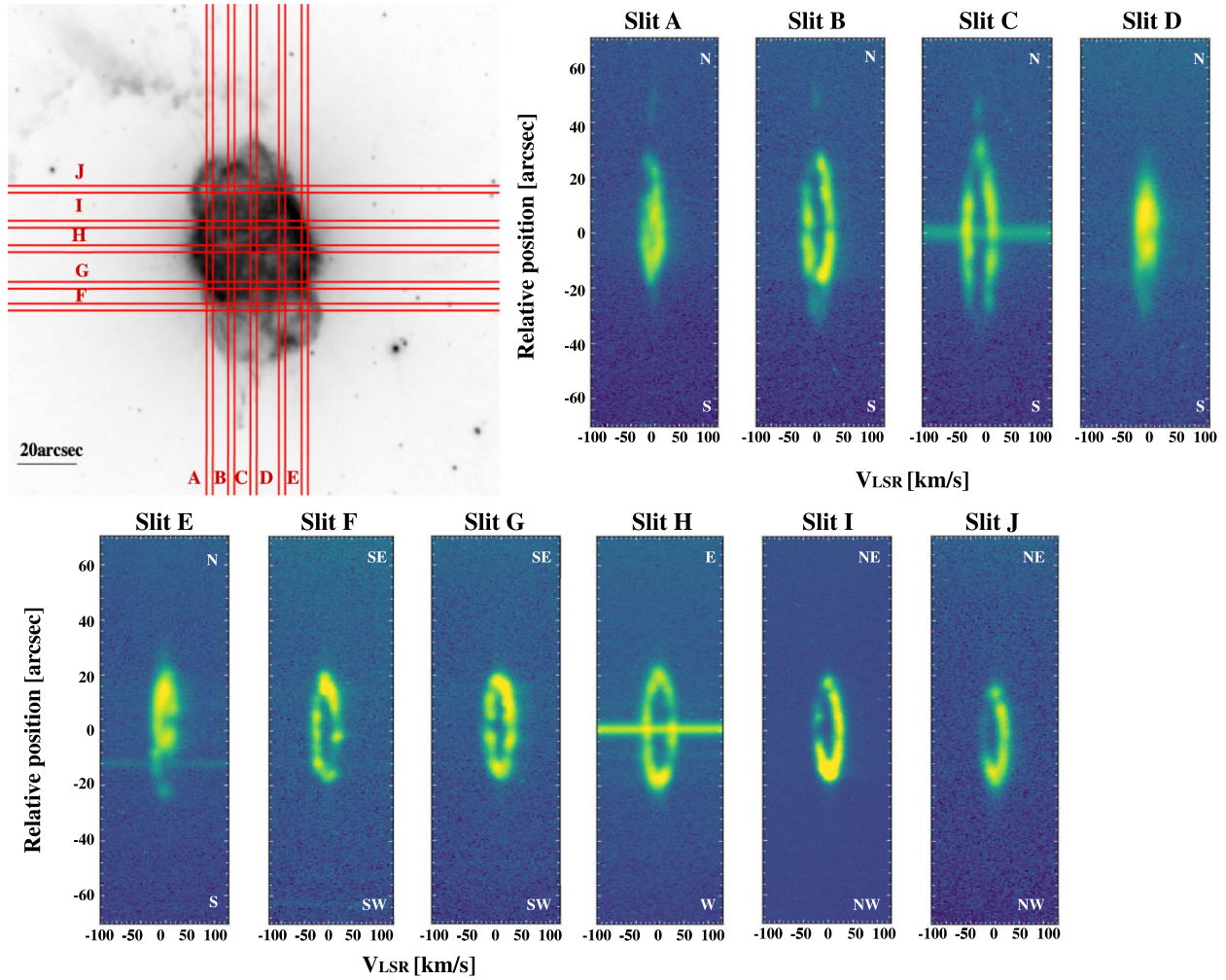


Figure 5. SPM MES [S II] 6716 Å spectra of NGC 40 obtained during 2019 September and October.

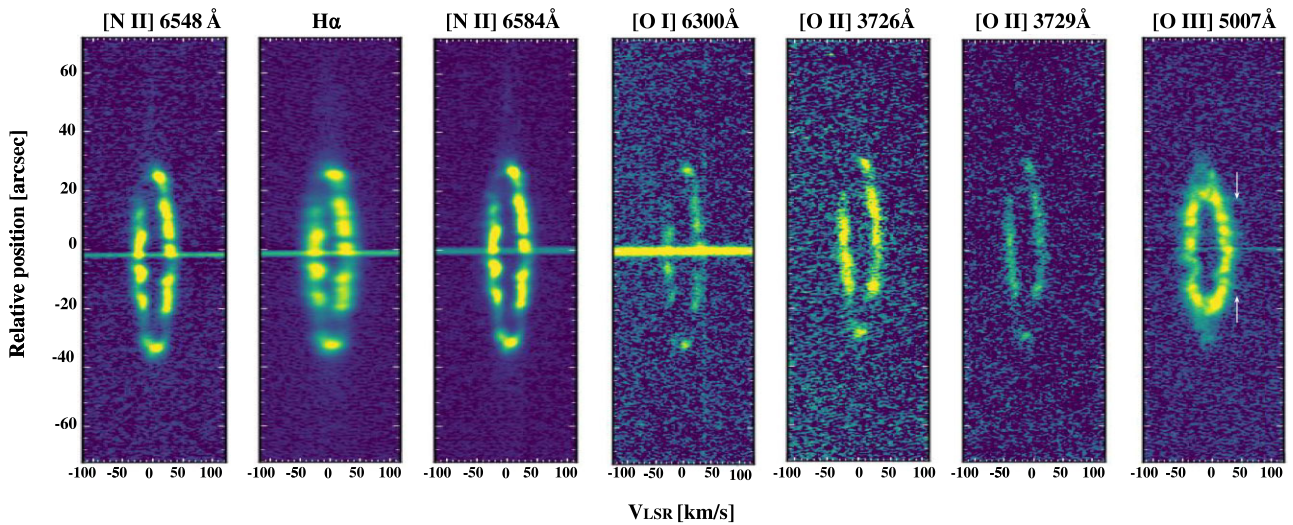


Figure 6. WHT UES spectra of NGC 40 taken with different filters. All spectra were obtained with a PA = 20°. Arrows in the [O III] PV (rightmost panel) indicate high velocity components (see Fig. 7 and the discussion section for details).

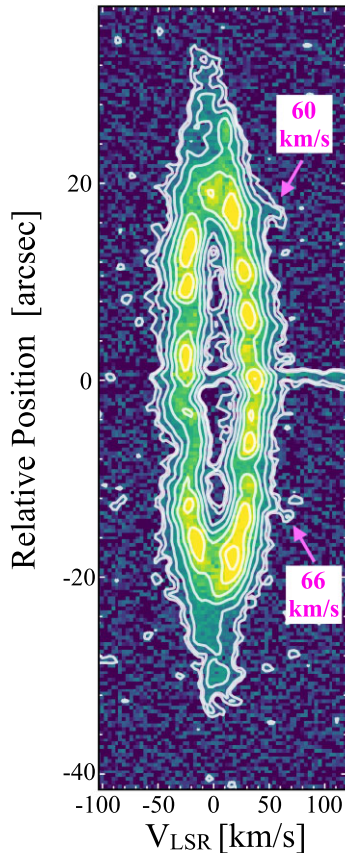


Figure 7. WHT UES [O III] 5007 Å PV of NGC 40 at PA = 20°. The (magenta) arrows show the high-velocity structures. The northern and southern structures have velocities of 60 and 66 km s⁻¹, respectively.

Table 3. Details of the different components from NGC 40.

Component	r (arcsec)	v_{exp} (km s ⁻¹)	τ_k (yr)
Main cavity	13.5 × 18.4	25	6500 ± 900
NW lobe	8	14.6	4900 ± 600
NE lobe	7	15.5	4000 ± 500
SW lobe	11.3	27.7	3700 ± 500
SE lobe	9.8	26	3800 ± 600

and [O II] images, but clear differences when compared with the [O I] and [O III] narrow-band images. We corroborated previous findings that the [O III] emission is contained within the cavity mapped by the H α emission line (see Meaburn et al. 1996, and references therein), whereas the [O I] emission is the most extended. This stratification can be easily explained by a ionization structure, with the highest ionized material (O⁺⁺) inside.

Moreover, NGC 40 appears to be composed by clumps and filaments and this turbulent pattern seems to have different origins depending on the ionization characteristics of the material. The clumps and filaments in the [O I], [O II], and [O III] images are not similar between them and have different shapes and sizes. To assess these morphological differences, we used the ASTRODENDO python package⁴ that provides a way to quantify the clumps and filaments in 2D images. The analysis of the three oxygen images

⁴For details see <https://dendrograms.readthedocs.io/en/stable/>

resulted in averaged clump sizes of 13.9, 24.0, and 16.9 arcsec² for the [O I], [O II], and [O III] images, respectively. Such morphological differences seem to be a consequence of the wind–wind interaction model of formation of PNe. As stated before, the fast wind from HD 826 (~ 1000 km s⁻¹) is slamming the slow wind ejected in a previous evolutionary phase producing hydrodynamical instabilities that can be seen as clumps in the O⁺⁺ image. These clumps and filaments prevent the material in the outer shells to be uniformly photoionized, creating streaks of alternate ionization regions that are detected in optical images (see fig. 1 in Toalá et al. 2019), causing the outer layers to be partially ionized and turbulent.

The n_e map obtained using the narrow-band [S II] images suggests a gradient from the SW region of NGC 40 towards the SE region. We have inspected the independent [S II] narrow-band images to look for possible inconsistencies that could produce this gradient, but we did not find any notorious effect. On the other hand, the n_e map presented by Leal-Ferreira et al. (2011) suggest maximum values associated with the western and southern regions of the main cavity, but we note that their map has a lower spatial resolution than ours as a result of their sparse spatial coverage and interpolation technique. Otherwise these authors report values of $n_e = 1000$ –3000 cm⁻³, which are consistent with our results. The inner cavity of NGC 40 seems to have averaged $n_e = 2000$ cm⁻³, with the highest values of 3500 cm⁻³ at the SW regions.

5.1 Multiple ejections in NGC 40

The optical data presented here suggest that HD 826, the CSPN of NGC 40, has experienced a number of successive mass-loss ejections. The NOT images of Fig. 1, along with the resultant ratio images presented in Fig. 3, unveil the presence of blowout structures protruding from the main cavity of NGC 40. These seem to correspond to two pairs of bipolar ejections aligned with PA of 80° and 135° corresponding to Axis 1 and 2 as defined in the bottom right-hand panel of Fig. 1, respectively. The ejections along Axis 1 seem to have pierced through NGC 40, but the ejections aligned along Axis 2 appear to be currently disrupting the main cavity producing small blisters structures. Surprisingly, the diffuse X-ray emission filling NGC 40 also have two maxima along these directions.

In accordance with Meaburn et al. (1996), we neither detect any hint of velocity pattern from the jet-like features 1N, 1S, 2N nor 2S (see Fig. 1). The increase by a factor of ~ 3 of the [O III]/H α ratio along the direction of the southern jet-like feature disclosed by the map presented in Fig. 3 (top-left panel) might be attributed to the effects of a jet piercing the SW cap of NGC 40 related to feature 1S. If the 1S structure were indeed a jet, it had to be contained within the plane of the sky.

Its possible counterpart, the 1N feature, is even more difficult to evaluate. We also do not find any velocity pattern for the structures defined as 2N–2S in Fig. 1. In fact, these features are reproduced by our SHAPE model as the intersection of the two pairs of northern and southern caps from the main barrel-like cavity of NGC 40.

Finally, there are two high velocity features detected in the [O III] WHT UES spectrum located inside the main cavity of NGC 40. These are detected at velocities ≈ 60 km s⁻¹ with no apparent counterparts in blue velocities. These inner high-velocity structures resemble the clumps detected in the IR images of NGC 40 presented by Toalá et al. (2019). It is quite possible that these structures are actually part of a quadrupolar configuration (two pairs of jets), but their blue counterparts would be self-absorbed by the nebula. Alternatively, we do not detect these high velocity components due to the limited

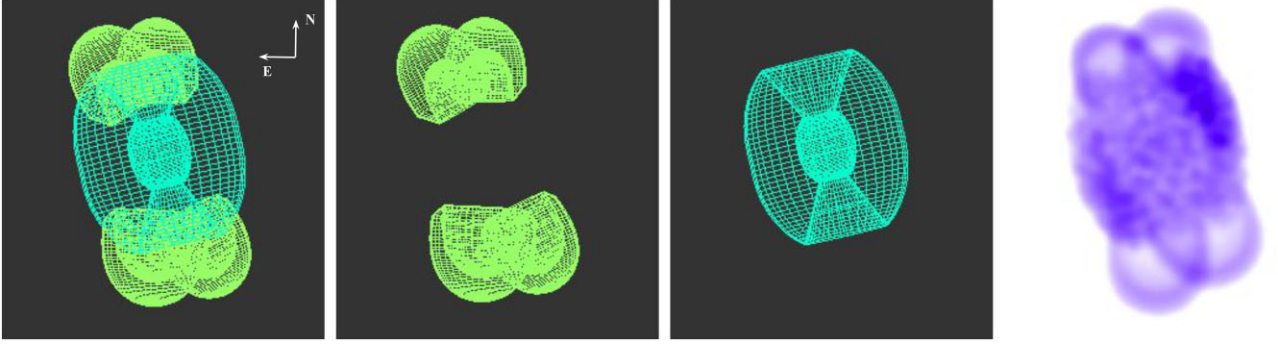


Figure 8. Components used in SHAPE model to reproduce the SPM-MES spectra of NGC 40. The rightmost panel shows a rendered synthetic image of the model.

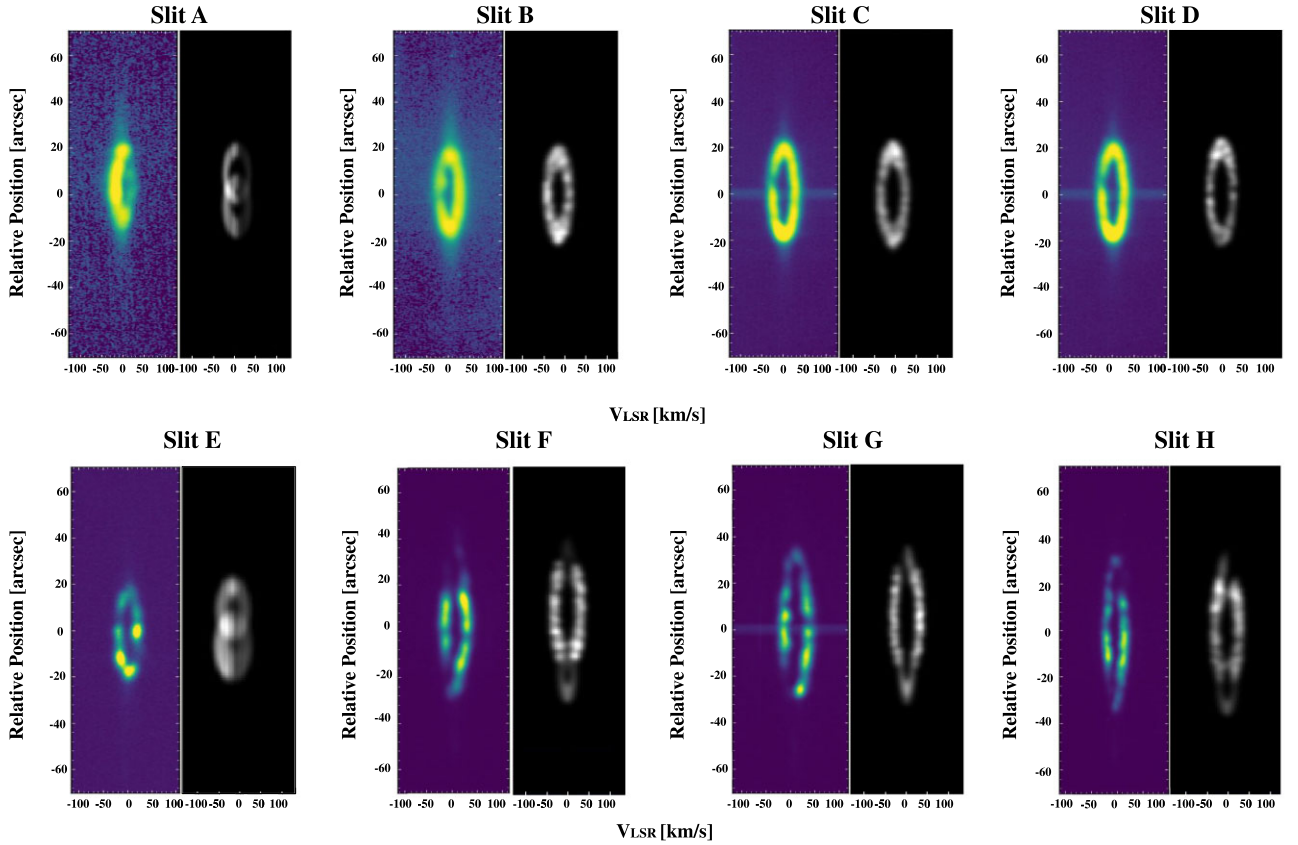


Figure 9. Synthetic PV diagrams obtained from our SHAPE model of NGC 40 (grey-scaled panels) compared with SPM-MES [N II] 6584 Å observations obtained on December 2013 and shown in Fig. 4 (coloured panels).

depth of the observations. Similar velocities have been detected from internal hydrogen-poor clumps in born-again NPs A 30, A 78 and HuBi 1 (Fang et al. 2014; Meaburn et al. 1998; Rechy-García et al. 2020). It is accepted that these clumps have been ejected during the VLTP, which reinforces the suggestion of Toalá et al. (2019) that NGC 40 belongs to this rare class of PNe.

5.2 Formation scenario of NGC 40

The spatio-kinematic model presented in Section 4 can be used to envisage the formation history of NGC 40. Since we have the expansion velocity v_{exp} of the different structures in NGC 40, we can

calculate their kinematic ages by following the equation:

$$\tau_{\text{k}} \approx 4744 \left(\frac{r}{\text{arcsec}} \right) \left(\frac{d}{\text{kpc}} \right) \left(\frac{v_{\text{p}}}{\text{km s}^{-1}} \right)^{-1} \text{ yr},$$

where r is the radius of each structure, d is the distance to NGC 40, and v_{p} is the deprojected rate of expansion. Since the inclination of NGC 40 with respect to the plane of the sky is virtually zero, $v_{\text{p}} \approx v_{\text{exp}}$. The estimated distance using data from *Gaia* data to NGC 40 is 1.87 kpc (Bailer-Jones et al. 2018). The estimated kinematic ages of each component are listed in Table 3.

The barrel-like main cavity of NGC 40 is the oldest structure in this PN with an kinematical age of almost 6500 yr. Other determinations of kinematic ages in the literature are consistent with this value.

Koesterke, Dreizler & Rauch (1998) report a kinematic age for the nebula of ~ 4000 yr considering a distance of 986 pc and Monteiro & Falceta-Goncalves (2011) find an age of 3500 ± 500 yr using a distance of 1.28 kpc.

The four caps in our morpho-kinematic model of NGC 40 have slightly different kinematical ages with the northern caps having larger τ_k values. However, considering the errors in their age determinations, these were probably formed by two contemporaneous bipolar ejections $\approx 4100 \pm 550$ yr ago. This situation is common in binary scenarios (see Guerrero et al. 2020). Numerical models that simulate bipolar PN formation using common envelope theory confirm it. For example, Zou et al. (2020) reported that, when considering cooling to the low-momentum flow in an adiabatically evolving lobe, we will obtain asymmetric bipolar nebulae where one lobe will have a greater extension, as observed in NGC 40.

The rest of the bipolar ejections discovered and reported in this paper are younger than the kinematic ages of the main cavity and lobes in NGC 40. In particular, the clumps detected in the WHT UES [O III] spectrum were ejected approximately 2000–2600 yr ago, which makes their formation by VLTP feasible and adding NGC 40 to the selected group of born-again PNe.

Considering all the structures unveiled by the present work, we can undoubtedly say that NGC 40 has experienced several episodes of mass ejection, making it a more complicated object than previously thought. Ring-like structures in the halo of NGC 40 have been found through optical and IR observations (Corradi et al. 2004; Ramos-Larios et al. 2011), which can be interpreted as evidence of a binary system at the core of NGC 40 (see e.g. Mastrodemos & Morris 1999). Binarity is the most likely formation mechanism to explain most features in PNe (Soker 1997; De Marco 2009), even scenarios in which the binary system enters a common envelope evolution (e.g. Ivanova et al. 2013; Zou et al. 2020; García-Segura, Taam & Ricker 2021). However, the multiple ejections with (at least) four different axis challenge these ideas. Other possibility could be the presence of a triple system (e.g. Soker & Bear 2021, and references therein), but it is expected that such systems produce more messy PNe, which is not the case of NGC 40.

There are other clear examples of PNe that still challenge our understanding of PNe formation mechanisms. For example, IC 4593 harbours several jet-like clumps along orthogonal directions (Corradi et al. 1997). Recently, Henney et al. (2021) thoroughly demonstrated that NGC 6210 has five symmetry axes and clear asymmetries. Objects like these, including now NGC 40, urges us to further peer into the formation mechanisms of PNe and very specifically on the chaotic final phases of the binary evolution through a common envelope.

6 SUMMARY AND CONCLUSIONS

We have presented the analysis of narrow-band images and high-resolution spectra of the Bow-tie Nebula, a.k.a. NGC 40, to produce a morpho-kinematic study of this PNe. We found a complex distribution of the ionization structure produced by turbulent structures caused by a combination of hydrodynamical and shadowing instabilities.

Our morpho-kinematic model of NGC 40 obtained with SHAPE helped us to assess the kinematic ages of the major morphological components of this PNe. At an adopted distance of 1.9 kpc, the main cavity has a kinematic age of 6500 yr. The northern and southern lobes, which are modelled with cap-like structures, seem to have been ejected 4200 yr ago.

We found four jet-like ejections aligned in different directions. Our images and spectra showed that some of these jet-like features have pierced NGC 40 in four regions at the main cavity, with an extra jet-like feature that has pierced the SE lobe. The youngest ejections are detected inside the main cavity of NGC 40 with higher velocities of 60 km s^{-1} . The youngest internal ejections seem to be in line with the VLTP event experienced recently by this PN proposed by Toalá et al. (2019).

We conclude that NGC 40 had a complex formation scenario involving multiple mass-loss episodes, some of them even not aligned with the main symmetry axis of this nebula. Multi-axis PNe such as IC 4593, NGC 40, and NGC 6210 challenge the current paradigm of PN formation.

ACKNOWLEDGEMENTS

The authors thank the referee for comments and suggestions that improved the presentation of our results. JBRG thanks Consejo Nacional de Ciencias y Tecnología (CONACyT, Mexico) for research student grant. JBRG and JAT thank funding by Dirección General de Asuntos del Personal Académico (DGAPA) of the Universidad Nacional Autónoma de México (UNAM) project IA100720. JAT thanks the Marcos Moshinsky Foundation (Mexico). JAT and GR-L acknowledge support from CONACyT (grant 263373). LS acknowledges a grant UNAM-PAPIIT IN101819 and IN110122 (Mexico). MAG is funded by the Spanish Ministerio de Ciencia, Innovación y Universidades (MCIU) grant PGC2018-102184-B-I00, co-funded by FEDER funds. MAG acknowledges support from the State Agency for Research of the Spanish MCIU through the ‘Center of Excellence Severo Ochoa’ award to the Instituto de Astrofísica de Andalucía (SEV-2017-0709). JAL acknowledges a grant DGAPA-PAPIIT IN103519 (Mexico) CONACyT A1-S-15140.

The data presented here were obtained in part with ALFOSC, which is provided by the Instituto de Astrofísica de Andalucía (IAA) under a joint agreement with the University of Copenhagen and NOT. This study is partially based upon observations carried out at the Observatorio Astronómico Nacional on the Sierra San Pedro Mártir (OAN-SPM), Baja California, Mexico. The authors thank the telescope operator P.F. Guillén for valuable guidance during several observing runs. This work has made extensive use of NASA’s Astrophysics Data System.

DATA AVAILABILITY

The data underlying this article will be shared on reasonable request to the corresponding author.

REFERENCES

- Acker A., Neiner C., 2003, *A&A*, 403, 659
 Aller A., Vázquez R., Olgún L., Miranda L. F., Ressler M. E., 2021, *MNRAS*, 504, 4806
 Arthur S. J., Hoare M. G., 2006, *ApJS*, 165, 283
 Bailer-Jones C. A. L., Rybizki J., Foesneau M., Mantelet G., Andrae R., 2018, *AJ*, 156, 58
 Balick B., 1987, *AJ*, 94, 671
 Chu Y.-H., Jacoby G. H., Arendt R., 1987, *ApJS*, 64, 529
 Clegg R. E. S., Seaton M. J., Peimbert M., Torres-Peimbert S., 1983, *MNRAS*, 205, 417
 Corradi R. L. M., Schwarz H. E., 1995, *A&A*, 293, 871
 Corradi R. L. M., Guerrero M., Manchado A., Mampaso A., 1997, *New Astron.*, 2, 461

- Corradi R. L. M., Sánchez-Blázquez P., Mellema G., Gianmanco C., Schwarz H. E., 2004, *A&A*, 417, 637
- Crowther P. A., De Marco O., Barlow M. J., 1998, *MNRAS*, 296, 367
- De Marco O., 2009, *PASP*, 121, 316
- Fang X. et al., 2014, *ApJ*, 797, 100
- Fang X., Zhang Y., Kwok S., Hsia C.-H., Chau W., Ramos-Larios G., Guerrero M. A., 2018, *ApJ*, 859, 92
- García-Rojas J., Peña M., Morisset C., Delgado-Inglada G., Mesa-Delgado A., Ruiz M. T., 2013, *A&A*, 558, A122
- García-Segura G., Taam R. E., Ricker P. M., 2021, *ApJ*, 914, 111
- Guerrero M. A., De Marco O., 2013, *AAP*, 553, A126
- Guerrero M. A., Miranda L. F., Riera A., Velázquez P. F., Olgún L., Vázquez R., Chu Y.-H., Raga A., Benítez G., 2008, *ApJ*, 683, 272
- Guerrero M. A., Toalá J. A., Medina J. J., Luridiana V., Miranda L. F., Riera A., Velázquez P. F., 2013, *A&A*, 557, A121
- Guerrero M. A., Ramos-Larios G., Toalá J. A., Balick B., Sabin L., 2020, *MNRAS*, 495, 2234
- Guerrero M. A., Cazzoli S., Rechy-García J. S., Ramos-Larios G., Montoro-Molina B., Gómez-González V. M. A., Toalá J. A., Fang X., 2021, *ApJ*, 909, 44
- Henney W. J., López J. A., García-Díaz M. T., Richer M. G., 2021, *MNRAS*, 502, 1070
- Hiltner W., Schild R., 1996, *ApJ*, 143, 770
- Ivanova N. et al., 2013, *A&AR*, 21, 59
- Jacob R., Schönberner D., Steffen M., 2013, *A&A*, 558, A78
- Koesterke L., Dreizler S., Rauch T., 1998, *A&A*, 330, 1041
- Kwok S., Purton C. R., Fitzgerald P. M., 1978, *ApJ*, 219, L125
- Leal-Ferreira M. L., Gonçalves D. R., Monteiro H., Richards J. W., 2011, *MNRAS*, 411, 1395
- Luridiana V., Morisset C., Shaw R. A., 2015, *AAP*, 573, A42
- Mastromedios N., Morris M., 1999, *ApJ*, 523, 357
- Meaburn J., Lopez J. A., Bryce M., Mellema G., 1996, *A&A*, 307, 579
- Meaburn J., Lopez J. A., Bryce M., Redman M. P., 1998, *AAP*, 334, 670
- Meaburn J., Lopez J. A., Gutiérrez L., Quiróz F., Murillo J. M., Valdéz J., Pedrayez M., 2003, *Rev. Mex. Astron. Astrofis.*, 39, 185
- Medina S., Peña M., Morisset C., Stasińska G., 2006, *RMxAA*, 42, 53
- Monteiro H., Falceta-Goncalves D., 2011, *ApJ*, 7348, 174
- Montez R., Kastner J. H., De Marco O., Soker N., 2005, *ApJ*, 635, 381
- Peña M., Rechy-García J. S., García-Rojas J., 2013, *RMxAA*, 49, 87
- Pottasch S. R., Bernard-Salas J., Beintema D. A., Feibelman W. A., 2003, *A&A*, 409, 599
- Ramos-Larios G., Phillips J. P., Cuesta L. C., 2011, *MNRAS*, 411, 1245
- Ramos-Larios G. et al., 2018, *MNRAS*, 475, 932
- Ramstedt S. et al., 2020, *A&A*, 640, A133
- Rechy-García J. S. et al., 2020, *ApJ*, 903, L4
- Sabbadin F., Hamzaoglu E., 1982, *AAP*, 109, 131
- Sabin L. et al., 2017, *MNRAS*, 467, 3056
- Soker N., 1997, *ApJS*, 112, 487
- Soker N., Bear E., 2021, *MNRAS*, 505, 4791
- Steffen W. et al., 2011, *IEEE Trans. Visualization and Computer Graphics*, 17, 454
- Stute M., Sahai R., 2006, *ApJ*, 651, 882
- Toalá J. A., Arthur S. J., 2016, *MNRAS*, 463, 4438
- Toalá J. A., Ramos-Larios G., Guerrero M. A., Todt H., 2019, *MNRAS*, 485, 3360
- Todt H. et al., 2015, 19th European Workshop on White Dwarfs, 493, 539
- Tody D., 1993, *Astron. Data Anal. Softw. Syst. II*, 52, 173
- Weidmann W. A. et al., 2020, *A&A*, 640, A10
- Williams R. J. R., 1999, *MNRAS*, 310, 789
- Zou Y. et al., 2020, *MNRAS*, 497, 2855

This paper has been typeset from a $\text{\TeX}/\text{\LaTeX}$ file prepared by the author.